Important Notice to Authors

Attached is a PDF proof of your forthcoming article in Optica Quantum. The article Manuscript ID is 573689. *No further processing of your paper will occur until we receive your response to this proof.*

Note: *Excessive proof corrections submitted by the author can result in significant delays to publication. Please include only essential changes that might be needed to address any shortcomings noticed in the proof-preparation process.*

Author Queries

Please answer these queries by marking the required corrections at the appropriate point in the text or referring to the relevant line number in your PDF proof.

Q1	AU: There is no mention of References [8, 45, 46 and 56] in the text. Please cite the references in the text. If no citation is supplied, we will delete the uncited reference from the list.
Q2	AU: The funding information for this article has been generated using the information you provided to us at the time of article submission. Please check it carefully. If any information needs to be corrected or added, please provide the full name of the funding organization/institution as provided in the Crossref Open Funder Registry (https://search.crossref.org/funding).

Other Items to Check

- Please note that the original manuscript has been converted to XML prior to the creation of the PDF proof, as described above. The PDF proof was generated using LaTeX for typesetting. The placement of your figures and tables may not be identical to your original paper.
- Please carefully check all key elements of the paper, particularly the equations and tabular data.
- Author list: Please make sure all authors are presented, in the appropriate order, and that all names are spelled correctly.
- Authors are responsible for registering their own ORCiD iDs. If you need to add ORCiD iDs for additional authors, please follow these steps. (1) First, log into your Optica account at account.optica.org. (2) Second, select “Participation” from the available headings on the login page, and then use the ORCiD iD widget to enter your number or register a new ORCiD iD.
- If figures need to be replaced because of accuracy or clarity concerns, please upload each revised figure as an individual PDF at the desired final size. In your corrections, please describe briefly what in the figure(s) has been changed.

OPTICA QUANTUM

Tunable quantum frequency conversion enabled by intermodal nonlinearity in optical fiber

K. Alexander,[1,†,*] T. Ulvenberg,[1,†] P. Wyborski,[1] C. Piccinini,[1] N. Gregersen,[1] B. Munkhbat,[1] R. H. Jensen,[2] L. Stefan,[2] P. Lodahl,[2,3] J. G. Koefoed,[4] M. Galili,[1] L. Rishøj,[1] and K. Rottwitt[1]

[1]*Department of Electrical and Photonics Engineering, Technical University of Denmark, 2800 Kongens Lyngby, Denmark*
[2]*Sparrow Quantum, Blegdamsvej 104A, 2100 Copenhagen, Denmark*
[3]*Center for Hybrid Quantum Networks (Hy-Q), Niels Bohr Institute, University of Copenhagen, Blegdamsvej 17, 2100 Copenhagen, Denmark*
[4]*NKT Photonics A/S, Bregnerødvej 144, 3460 Birkerød, Denmark*
[†]*These authors contributed equally to this work.*
**kahea@dtu.dk*

Received 15 July 2025; revised 5 October 2025; accepted 20 October 2025; published 0 Month 0000

Optical frequency conversion plays a key role in realizing large-scale quantum networks, including multi-qubit discrete-variable quantum computers and quantum communication links where photons serve as the fundamental qubits. However, achieving efficient conversion via nonlinear optical processes for specific target wavelengths remains a significant challenge, as precise dispersion control is essential to satisfy phase-matching conditions across specific frequency ranges. An intriguing approach to solve this challenge is leveraging the modal degree of freedom in spatially multimoded waveguides and realizing intermodal nonlinear interaction. Following this approach, we present the experimental demonstration of tunable, number-state-preserving frequency conversion of true single photons emitted from a quantum dot. The conversion is achieved in a multimode fiber and exhibits a peak internal efficiency of 85% while retaining single photon purity of 99% during conversion. Our results show that the intermodal platform presents a promising and versatile approach for overcoming phase-matching limitations in quantum frequency conversion, thus allowing the efficient interfacing of different optical quantum devices.

https://doi.org/10.1364/OPTICAQ.573689

1. INTRODUCTION

Many applications within quantum optics, including emerging technology such as quantum computing [1,2], quantum communication [3,4], and quantum cryptography [5], rely on the interference of single-photon-level optical quantum states at various positions in a quantum network. For example, quantum interference effects are exploited for the preparation of entangled resource states in measurement-based quantum computing [6,7]. However, these effects require that interfering photons be identical. While single-photon sources based on semiconductor quantum dots (QD), the workhorse for pure quantum state generation within quantum optics, routinely demonstrate photon indistinguishability exceeding 0.96 [8,9] for photons emitted from the same source, the typical inhomogeneous broadening of QDs is 10–50 nm. Additionally, for monolithic cavity-based sources [9], fabrication imperfections cause uncontrolled variations in the cavity resonance frequency from device to device, resulting in small frequency variations between photons emitted from different devices. Overcoming the challenge of spectral distinguishability between photons from different sources would be a significant step towards realizing scalable quantum optics protocols that utilize high-visibility multi-photon interference.

Quantum frequency conversion (QFC) presents one avenue towards achieving this, as it allows the fine-tuning of photons from different devices into resonance, thus realizing mutual indistinguishability between different sources. Several schemes are capable of QFC while preserving quantum properties (such as non-classical number statistics). Small sub-nanometer wavelength shifts can, for instance, be achieved by exploiting optomechanical effects [10] or electro-optical modulation [11], while larger shifts are enabled by nonlinear parametric processes such as sum/difference frequency generation (three-wave mixing, TWM) [12–16] and Bragg scattering four-wave mixing (BS-FWM) [17–21]. In these nonlinear parametric processes, strong laser beams (called pumps) are used to mediate energy transfer between much weaker optical fields by exploiting the nonlinear response of a medium through which the light propagates. TWM has notably been used to demonstrate the interfacing of distinct single-photon emitters over 300 km of fiber by initially converting their output to the low-loss telecom band [16]. However, the process requires the use of a specialized pump laser source and is inherently limited to large frequency shifts. In contrast, FWM is driven by two optical pumps, and this also allows for precise wavelength tuning even down to the nanome-

ter and sub-nanometer scale [20,22]. Moreover, the additional pump offers further ways of tailoring the conversion process to specific needs, such as tunability in the output frequency and output spectro-temporal profile [23], which can be used in optimizing the shape of a single-photon wave packet prior to interaction with a line-shape-sensitive quantum computational device such as a quantum memory. Finally, as FWM occurs naturally in standard optical fibers (as opposed to TWM), it can be integrated into existing low-loss transmission networks and can benefit from long nonlinear interaction lengths. Recent work on BS-FWM for fiber-based QFC has included efforts in progressing design, fabrication and implementation for systems based on photonic crystal fiber (PCF), as this platform offers highly nonlinear fibers with engineerable dispersion properties that can be tailored to allow QFC at specific desired wavelengths [24–26]. Recently, the use of polarization mode dispersion to achieve phase matching has also been demonstrated by employing cross-polarized pumps in a birefringent fiber. This way, frequency up- and down-conversion of broadband heralded single photons between pairs of specific wavelengths was demonstrated with near-unity efficiency, but with limited wavelength tunability [27].

An alternative yet likewise versatile approach to accessing new wavelength regions for QFC is the multimode platform. Rather than relying on dispersion engineering to target specific wavelengths, this approach exploits intermodal nonlinear interactions, thus leveraging the distinct dispersion properties inherent in various spatial modes that form the transverse solutions to Maxwell's equations in optical waveguides above the single-mode cut-off [28]. This approach extends dispersive degrees of freedom with minimal additional engineering, requiring only a shift in the single-mode cut-off to enable higher-order mode propagation at target wavelengths. A key advantage of this intermodal approach is its straightforward implementation in simple step-index fibers with sufficiently large core diameters and numerical apertures (NA). Beyond offering an additional modal degree of freedom, these multimode fibers come with all the practical advantages of robust solid-core step-index silica fibers: easy coupling and splicing as well as low bending- and transmission loss [29]. Previously, we demonstrated the advantages of this multimode fiber platform for frequency conversion in the classical regime [22,30,31]. In this work, we extend its application to the quantum regime, presenting the use of intermodal processes for highly efficient, low-noise frequency conversion of true single photons emitted by a QD. We show that the conversion process is tunable within a 5 THz spectral window and that it exhibits a peak internal conversion efficiency of 85%. This marks a significant step toward realizing the full potential for QFC of the fiber-based multimode platform, which offers substantial advantages by combining key features from 3 separate components: (1) the tunability of four-wave mixing, (2) the flexibility, robustness, and low transmission loss of optical fibers, and (3) the added dimensionality of multimode light propagation, which ultimately enables unprecedented QFC bandwidths spanning the emission range of multiple single-photon sources [32], as we shall show in the following.

2. METHODS

2.1. Theory and Principle of the Intermodal Approach

To highlight the significant advantages of the multimode fiber platform for QFC, it is essential to consider the fundamentals of BS-FWM. The theory of QFC via BS-FWM has been covered in detail in previous papers [23,33–35], and additional details specific to the application presented here are found in Supplement 1. In brief, the semi-classical treatment of BS-FWM with co-polarized fields in optical fibers considers the coupled evolution of quantum *signal* and *idler* (s and i), under the influence of (classical) co-propagating pumps (p and q). As sketched in the transition diagram in Fig. 1(a), the BS-FWM process involves the simultaneous annihilation of one p and s photon and the creation of one q and i photon—effectively leading to the coherent transfer of energy from s to i. While the generation of i is the intended outcome of the BS-FWM process, it is here referred to as the idler, in keeping with established nomenclature within the study of parametric nonlinear interactions. In contrast to parametric amplification, the BS-FWM process preserves the photon number in the quantum band [17] and does not add additional noise photons. This means that for a single photon input state, the BS-FWM process translates the non-classical number statistics of the input state, s, to the output state, i. These properties make BS-FWM suitable for QFC.

Momentum conservation in the BS-FWM process requires that $\mathbf{k}_\mathrm{p} + \mathbf{k}_\mathrm{s} = \mathbf{k}_\mathrm{i} + \mathbf{k}_\mathrm{q}$, where $\mathbf{k}_n$ denotes the wave vector of each field involved in the interaction. This condition, known as phase matching, must be fulfilled to maximize the efficiency of the conversion process. In this regard, the multimode platform offers significant advantages over its single-mode counterpart, as the additional modal degrees of freedom provide enhanced flexibility. In a multimode waveguide, each mode is characterized by a distinct spatial distribution of the electromagnetic field. Due to their different field distributions, individual modes experience slightly different optical phase evolution as they propagate through the waveguide structure, governed by their respective wave vectors. In fiber optics, where light propagation occurs along one axis, this behavior is characterized by a mode-specific propagation constant, β. This added dimensionality allows intermodal BS-FWM to be successfully phase matched by simply choosing proper propagating modes for the various fields. In contrast, the phase-matching requirement in single-mode systems is usually only satisfied by diligent engineering to tailor the dispersion profile of the single allowed mode. Consequently, the design and fabrication of additional waveguides is often required for each new wavelength region [36]. The advantage of the intermodal approach is therefore evident: if the fundamental mode of a multimode system does not permit phase matching at the desired wavelength configurations, an alternative combination of modes may provide a viable solution, as exemplified in the following. This work considers intermodal processes in which the *signal* and *idler*, as well as the pumps p and q, occupy pairwise identical transverse modes. In this case, phase matching is achieved when the inverse of the group velocity, $\beta_1 \equiv v_g^{-1}$, at the average frequency of the two pumps is identical to that at the average signal and idler frequency. On a wavelength axis, as in Fig. 1, the wavelengths corresponding to these average frequencies are referred to as central wavelengths. See more details in Supplement 1. As illustrated in Fig. 1(b), this means that in a conventional multimode step-index fiber, two readily available telecom pump lasers confined to the narrow telecom band (~1570 nm) can support phase-matched frequency conversion within a much wider spectral band in the higher frequency range spanning from below 750 nm to above 1050 nm—if the propagation mode of the pump lasers is selected appropriately. Selecting spatial modes of increasingly

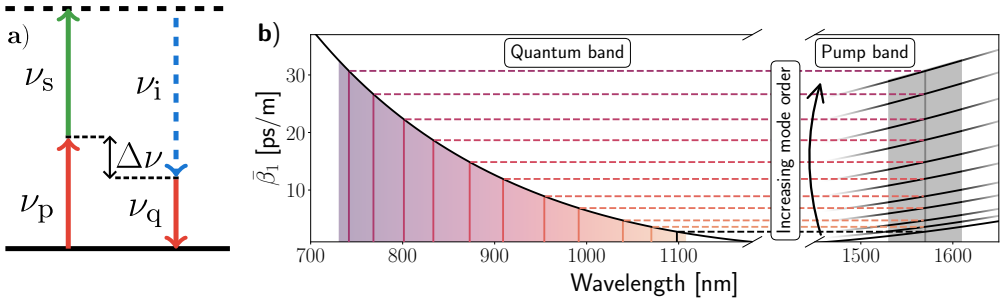

Fig. 1. (a) A transition diagram with a virtual excited state representing the BS-FWM process. A pump, p, and a signal, s, photon is annihilated/absorbed under the simultaneous creation/emission of another pump, q, and an idler, i, photon. (b) The relative inverse group velocity, $\bar{\beta}_1$, as a function of wavelength is shown for the shorter-wavelength region, referred to as the "quantum band," and the longer-wavelength region, denoted the "pump band." The fiber in this example is a conventional step-index multimode fiber with a core radius of 25 μm and a numerical aperture (NA) of 0.22. In the quantum region, the relative inverse group velocity is plotted for the fundamental mode (black line), whereas in the pump region, it is plotted for the fundamental mode and 10 higher-order linearly polarized (LP) modes (the upper 10 black lines). The horizontal colored dashed lines connect the two central wavelengths in the quantum and pump bands, respectively, where intermodal phase matching is achieved for distinct BS-FWM processes. The phase-matched central wavelength for the pumps is 1570 nm for all processes. However, by simply increasing the pump mode order, the phase-matched central wavelength in the quantum band becomes progressively shorter—new spectral regions are accessed.

higher order for the telecom pumps leads to phase matching at increasingly shorter wavelengths for the quantum fields. For this purpose, a variety of methods already exist to efficiently couple light into specific targeted modes, e.g., mode-coupling gratings [37], photonic lanterns [38], binary phase plates [39], and spatial light modulators [40]. The broad wavelength region in Fig. 1(b) designated as the "quantum band" largely covers the entire emission range of typical high-performing QD-based single-photon sources (0.7–1.0 μm). In this example, only a subset of the modes supported by the fiber is considered; however, by accessing even higher mode orders, the wavelength range can be extended well below 750 nm. This, in essence, highlights the design flexibility offered by the intermodal approach. In principle, it offers a path towards realizing a monolithic platform for interfacing state-of-the-art quantum light sources based merely on commercially available telecom components and an off-the-shelf step-index fiber. It is noted that the type of BS-FWM process presented here, which couples the QD emission range with the telecom range, is agnostic to which frequency components are assigned to the pumps and which to the signal and idler. Thus, the processes are also capable of QFC within the telecom band as well as between the QD emission band and the telecom band.

2.2. Experimental Configuration and Setup

To demonstrate the intermodal BS-FWM platform, a specific intermodal process in a multimoded system is considered. The multimoded system is realized in a simple silica step-index fiber (see Fig. 2(a)) with a germanium-doped core of 19 μm in diameter and a numerical aperture (NA) of 0.12 [41]. The fiber guides the first two linearly polarized (LP) modes, namely LP_{01} and LP_{11}, across the entire telecom band, and will henceforth be referred to as the two-mode step-index fiber (TMSI). Figure 2(b) shows the inverse group velocity for the two LP modes, demonstrating that the intermodal phase-matching condition is satisfied for LP_{11} pumps at telecom wavelengths (specifically the L-band, ~1.60 μm) and LP_{01} quantum fields in the near-infrared band (~0.97 μm). The frequency separation between these two bands is referred to as the inter-band separation, which in this case is approximately 120 THz. The short-wavelength region of the quantum band is of specific interest as it overlaps the typical emission range of InAs-based QD sources [42,43]. As also shown in Fig. 2(b), the fundamental mode is not suitable as the pump mode, since wavelength conversion is then phase matched only above 1.0 μm—outside the target quantum band. A diagram of the process is sketched in Fig. 2(c), which shows the spatial mode distribution of the pumps (LP_{11}) and quantum components (LP_{01}) inside the TMSI, respectively. In accordance with energy conservation (see Fig. 1(a)), the size of the frequency shift (from input ν_s to output ν_i) is dictated by the detuning ($\Delta\nu$). As this is the common detuning between fields in the quantum and pump bands, respectively, it will be referred to as the intra-band detuning. Thus, the intermodal LP_{01}/LP_{11} BS-FWM process allows phase-matched frequency tuning of a broad class of quantum light sources mediated by spectrally far-detuned pumps with wavelengths in the telecom range. Other than allowing the use of readily available telecom lasers to drive the process, the substantial spectral isolation of the quantum fields from the classical band makes it trivial to suppress the noise in the spectral vicinity of the pumps which otherwise dominates the classical band (see Fig. 3(a)). This noise arises from effects such as amplified spontaneous emission in the pump amplifiers, spurious nonlinear interaction, and spontaneous Raman scattering. The latter would be especially detrimental to QFC were it not for the fact that the quantum fields are situated 120 THz into the anti-Stokes band of the pumps, where Raman scattering is negligible [35].

Figure 3 shows a sketch of the system used for the conversion of single photons via intermodal BS-FWM. Two pump waves are carved into 0.5 μs pulses using an acousto-optic modulator and amplified in a sequence of erbium-doped fiber amplifiers. The pulse carving increases the pump peak power at the cost of a reduced temporal overlap with the signal light, which constitutes a continuous stream of single photons emitted from an InAs QD under continuous-wave (CW) quasi-resonant excitation, or alternatively, continuous laser light emitted from a classical laser tuned to the QD emission wavelength. Note that since the phase-matching approach employed in this work relies on (inverse) group-velocity matching between the signal/idler and the two pumps, the walk-off between the components is

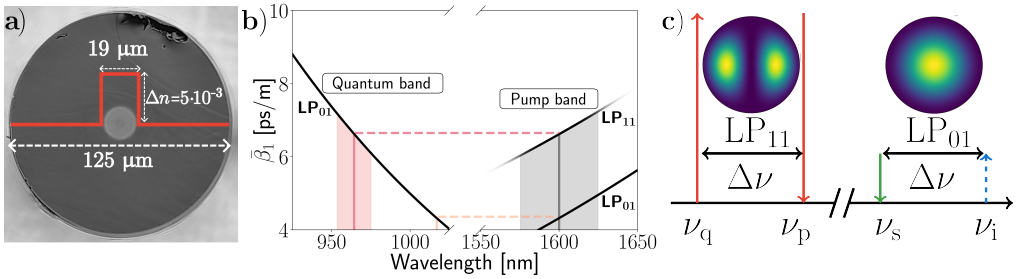

Fig. 2. (a) End-facet image of the two-mode step-index fiber (TMSI) used for the frequency conversion experiments. The refractive index contrast, Δn, is indicated for a wavelength of 632 nm. (b) The inverse group velocity of the first two guided linearly polarized (LP-) modes in the TMSI relative to the inverse group velocity of the fundamental mode (LP_{01}) at the zero-dispersion wavelength. The horizontal dashed lines indicate group velocity matching at the average frequency (center wavelength) in the quantum and pump spectral bands, respectively. Only the process involving the LP_{11} mode is phase matched inside the desired quantum band. (c) Diagram of the (intermodal) BS-FWM process used in the experiments with simulated field distributions for the different modes. Energy is exchanged between two pumps of frequency ν_p and ν_q, while a single photon is (up-)converted from frequency ν_s to ν_i.

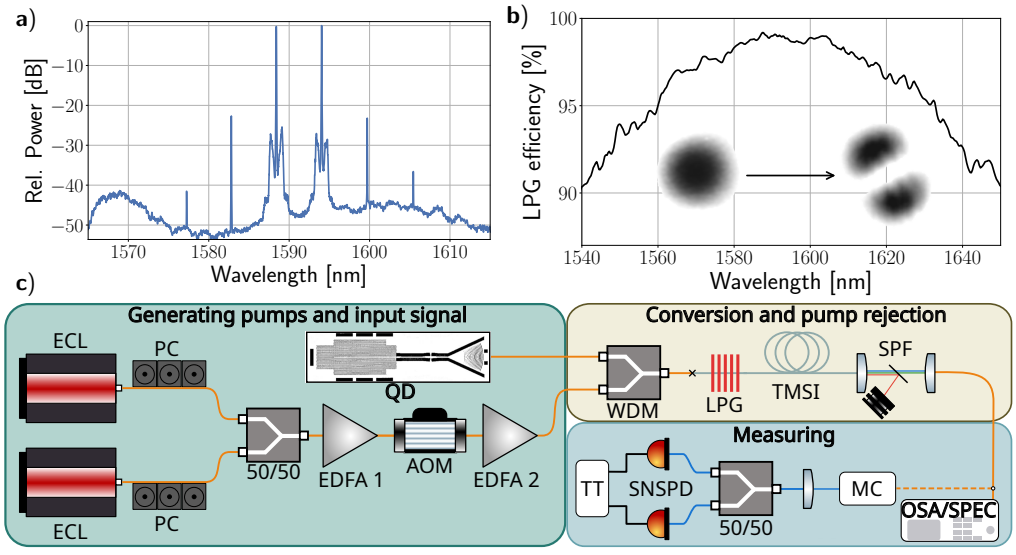

Fig. 3. (a) An example output pump spectrum for an intra-band detuning of 0.7 THz showing appreciable modulation instability in the pump band. The spectrum is normalized to the pump peak. (b) Mode conversion efficiency of the long-period grating (LPG) along with the intensity distribution of the two modes imaged at the fiber facet (the arrow indicates the conversion direction of the LPG). (c) Experimental setup for intermodal QFC: AOM, acousto-optic modulator; BD, beam dump; ECL, external cavity laser; EDFA, erbium-doped fiber amplifier; LPG, long-period grating; MC, monochromator; OSA, optical spectrum analyzer (for classical analysis); PC, polarization controller; QD, quantum dot; SPF, short-pass filter; SNSPD, superconducting nanowire single-photon detector; SPEC highly sensitive spectrometer (for quantum analysis); TMSI, two-mode step-index fiber; TT, time-tagger; WDM, wavelength-division multiplexer; 50/50 3 dB fiber coupler.

inherently minimized and remains below 0.1% of the pump pulse duration in our experiments. The single photon source used here consists of an InAs quantum dot (QD) embedded in a ~180-nm-thick GaAs membrane, which incorporates a built-in p-i-n diode, maintained at a temperature of 4 K. A bias voltage is used to stabilize the quantum dot charge state and suppress noise. The QD is positioned within a photonic crystal waveguide, enabling efficient photon routing. A 3D sketch of the photonic waveguide structure is included in Supplement 2. The excitation wavelength is tuned slightly below the QD emission wavelength (971.25 nm) for quasi-resonant/p-shell excitation. The beam of the excitation laser impinges on the QD perpendicularly to the sample plane. The resulting single photons emitted in-plane from the QD are guided through the photonic crystal waveguide to a shallow-etched grating coupler, which directs them out of the chip and ultimately into an optical fiber. From this fiber, the single photons are combined with the pump pulses using a fiber-based wavelength-division multiplexer before coupling into the TMSI. The pump peak power is estimated to be 6.75 W per pump at the input of the TMSI. With an efficiency of more than 97% (as seen in Fig. 3(b)), a thermally induced long-period fiber grating [37] converts the spatial mode of the pump pulses with wavelengths ~1.6 µm to the first higher-order LP mode, LP_{11}, inside the TMSI shown in Fig. 2(a). In the 930-m-long TMSI, frequency conversion of the signal (either single photons or coherent laser light) takes place. Both the input photons and the converted output photons propagate in the fundamental fiber mode, LP_{01}, which ensures phase matching for the desired process as per Fig. 2(b). After the conversion inside the TMSI, pump light is filtered away, and the remaining light in the quantum band is passed to either an optical spectrum analyzer for measurements in the classical regime or to a highly sensitive

few-photon-level spectrometer for measurements in the quantum regime. Finally, when characterizing photon number statistics, a monochromator is used to spectrally select either the signal or the idler photons and direct them to a beam splitter with output ports going to two superconducting nanowire single-photon detectors arranged in a Hanbury Brown and Twiss configuration for coincidence counting using a time tagger. Supplement 2 and Supplement 3 describe the setup and its components in detail. The wavelengths of the pumps driving the conversion process can be continuously and individually tuned across the entire bandwidth of the telecom L-band (1570–1610 nm). Consequently, the wavelength of the frequency converted idler is likewise continuously tunable within the range 965–980 nm.

3. RESULTS

3.1. Tunable Up- and Down-Conversion within Quantum Band

The typical figure-of-merit used to quantify the performance of a QFC process is the conversion efficiency, which is defined as the probability of successfully converting each signal photon. Since the signal and idler experience identical optical loss in the setup, this probability can be determined solely from the spectral composition of the output. The per-pump-pulse or *peak* internal conversion efficiency of the subset of signal photons that temporally overlap with the pumps is given by:

$$\eta_{\text{peak}} = \frac{1}{\text{DC}} \frac{\eta}{1+\eta}, \tag{1}$$

where DC is the duty cycle of the pump pulse carving, and η is the magnitude of the idler part relative to the signal part in the photon flux spectrum measured at the output. See Supplement 4 for details on the method used for extracting the conversion efficiency.

Figure 4(a) shows the spectra of single photons emitted by the QD. The solid black line shows the emission spectrum when the BS-FWM pumps are turned off. The recorded photon flux is normalized to the main peak situated at 971.25 nm, which is the peak targeted for the frequency conversion process. To check the stability of the QD emission spectrum, a total of 40 measurements, each with a 30-second integration time, were performed of this spectrum (i.e., without BS-FWM pumps) throughout the duration of the project. The shaded gray area marks the standard deviation of these measurements and shows that the spectral features of the QD emission (specifically, the location of side peaks) remain fixed when the BS-FWM pumps are turned off. When the BS-FWM pumps are turned on, however, a new side peak appears in the measured spectrum corresponding to frequency-converted single photons. We note also that no *spurious* side peaks are observed (above the background noise floor) in the measured output. This indicates that competing BS-FWM processes are efficiently suppressed in this system by at least *gt*;13 dB. We attribute this to the long fiber length and lack of phase matching for these competing BS-FWM processes, which arises from the nonzero local group velocity dispersion [44].

To investigate the tunability of the conversion process, experiments were carried out for multiple different settings of the intra-band frequency detuning, $\Delta\nu$. Each colored peak in Fig. 4(a) thus shows the spectrum of converted photons for a specific intra-band detuning. Figure 4(b) shows the corresponding conversion efficiency calculated using Eq. (1) with the colored data points matching each colored peak in Fig. 4(a). The black line shows a classical sweep of the conversion spectrum with a continuously tunable diode laser supplying the input signal instead of the QD. The dashed line shows a classical sweep of the redshifted part of the output spectrum after further optimization of the power distribution between the two pumps. This optimization was not performed for measurements in the quantum regime, leading to a slight spectral asymmetry. A detailed experimental analysis of the power scaling of the process is found in Supplement 5.

Both quantum and classical measurements in Fig. 4(b) exhibit a reduction in efficiency (η_{peak}) with increasing absolute intra-band frequency detuning. This is despite the degree of linear phase mismatch being minimized during experiments by diligently adjusting both pump wavelengths when varying the detuning. For an ideal fiber, the freedom to tune both pumps guarantees that phase matching can be maintained for the central wavelengths across the entire spectrum shown in Fig. 4. However, the phase-matching *bandwidth* of the process does narrow for increasing intra-band detuning. Separate experiments show that it contracts from ~10 GHz (FWHM) at a detuning of $|\delta\nu| =$ 0.6 THz to ~3 GHz at $|\delta\nu| = 2.4$ THz. Thus, for broadband signals, some reduction in efficiency is expected due to spectral clipping when the phase-matching bandwidth becomes narrower than the input linewidth. Even so, the fact that we observe the same decrease in efficiency for measurements in both the quantum regime (with typical QD emission linewidth ~1 GHz) and the classical regime (with input laser linewidth < 10 kHz) shows that the observed efficiency decay is not a direct expression of a narrowing phase-matching bandwidth, as the reduction is seen to apply identically for inputs with vastly different linewidths. Instead, we expect that the efficiency decrease for both quantum and classical measurements can primarily be attributed to various fiber-imperfections, e.g., core radius fluctuations [45], which lead to effects such as residual varying birefringence, rotation of the birefringence axis, random linear mode coupling, and randomly fluctuating effective refractive index for the different modes along the propagation axis [46–48]. These effects cannot be wholly compensated for by adjusting the pump wavelengths. For a given pump power, this imposes a practical limit on the intra-band conversion span. These adverse effects can be mitigated by increasing the nonlinear interaction strength, thus allowing the use of a shorter fiber. This can be achieved, for example, by using highly nonlinear fibers [49] or by employing higher pump powers. As stated previously, the phase-matching bandwidth at $|\delta\nu| = 2.4$ THz is ~3 GHz (FWHM), which is close to the typical QD linewidth. Consequently, as the intra-band detuning is increased even further, the phase-matching bandwidth will eventually become a limiting factor for the conversion of the QD single photons. In this regard, increasing the interaction strength and using shorter fibers also helps, as it expands the phase-matching bandwidth, which is inversely proportional to the interaction length.

3.2. Single-Photon Purity

To quantify the single-photon purity of the converted output, the second-order correlation function, $g^{(2)}(\tau)$, was measured by performing coincidence counting in the Hanbury Brown

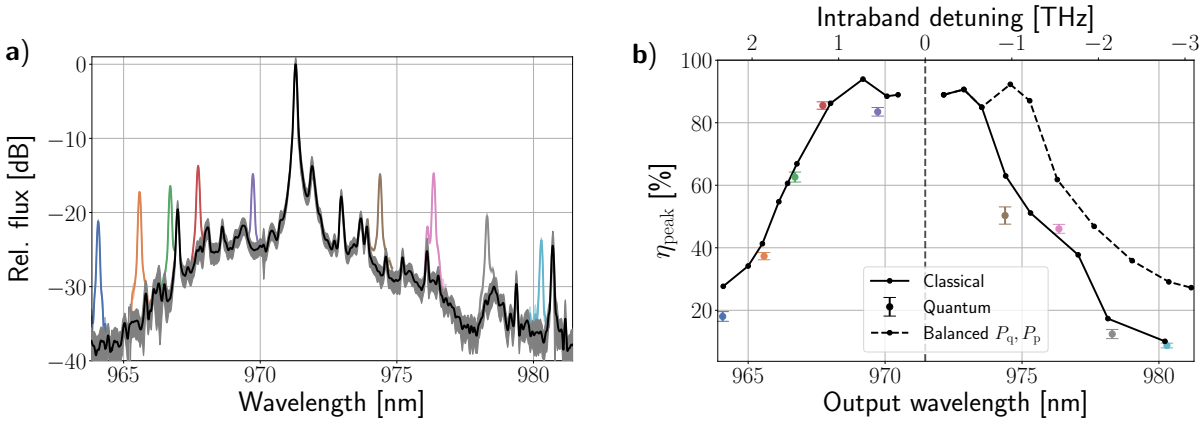

Fig. 4. (a) Output QD spectra measured by a highly sensitive spectrometer. The black line shows the QD spectrum based on the average of 40 measurements taken with the BS-FWM pumps turned off, and the shaded gray area indicates the standard deviation. Each colored peak shows the mean of five measurements of the spectra of converted photons taken with the BS-FWM pumps turned on, with central wavelength determined by the intra-band frequency detuning, as per Fig. 2(c). (b) The corresponding peak conversion efficiencies based on Eq. (1). The colored dots show the measured peak efficiency of converting the input single photons from the main QD peak to the wavelengths indicated by the corresponding colored peaks in (a). The standard deviation of the measurements is indicated by the vertical bars. The black line shows the conversion efficiency, η_{peak}, for measurements in the classical regime (i.e., with a CW laser acting as signal input), whereas the dashed line is the same classical measurement performed after further optimization of the optical power distribution between the pumps.

and Twiss setup [50] (see Fig. 3). The same characterization was performed on the photon flux emitted directly from the QD, which serves as a reference. The reference measurement of the second-order correlation function, seen in Fig. 5(a), displays clear anti-bunching for near-zero correlation times with $g^{(2)}(0) \ll 0.5$, which confirms that the QD is a single-photon emitter obeying sub-Poissonian number statistics. For nonzero correlation times on a scale of ~100 ns, weak bunching is observed as evidenced by a $g^{(2)}(\tau)gt; 1.0$. This bunching is a signature of minor blinking of the QD [51], possibly exacerbated due to the slightly non-resonant excitation scheme implemented. Importantly, the weak blinking and associated photon bunching bear no influence on the single-photon purity, which is evaluated based on the statistics at zero correlation time. To capture both anti-bunching and bunching effects, the reference measurement data is fitted to a double exponential of the form:

$$g^{(2)}_{\text{fit}}(\tau) = 1 - Ae^{-|\tau|/\tau_A} + Be^{-|\tau|/\tau_B}, \quad \textbf{(2)}$$

with τ_A (τ_B) being the characteristic timescale on which the anti-bunching (bunching) is observed. The value of $g^{(2)}_{\text{fit}}(0)$ and the covariance matrix of the fitting parameters provide the estimate and uncertainty of the value of the second-order correlation function at zero time delay for the input photons. Based on this, $g^{(2)}_{\text{in}}(0) = 0.010 \pm 0.005$. Figure 5(c) shows the same characterization of the second-order correlation function for the frequency converted output photons. For this specific measurement, an intra-band detuning of 0.67 THz was obtained. A clear dip at zero time delay is observed, and by fitting the data according to Eq. (2), it is found that $g^{(2)}_{\text{out}}(0) = 0.01^{+0.05}_{-0.01}$. Comparing $g^{(2)}_{\text{out}}(0)$ and $g^{(2)}_{\text{in}}(0)$, the results indicate minimal addition of spurious noise photons in the converted output, highlighting the noiseless and state-preserving property of frequency conversion via BS-FWM [17], which also applies for the intermodal variant. Assuming that potential background noise added by the QFC system is uncorrelated with the stream of single photons, and assuming the single photons are emitted from an ideal single-photon emitter (with $g^{(2)}_{\text{ideal}}(0) = 0$), the level of background noise can be estimated based on the measured $g^{(2)}$ [52]. With our estimator, $g^{(2)}_{\text{out}}(0) \approx 0.01$, the fraction of noise photons in the output is ~0.5% (same as the input). An upper limit of 3.4% noise photon pollution after conversion is found based on the upper bound estimate of $g^{(2)}_{\text{out}}(0) \leq 0.06$. The low level of noise photon pollution detected at room temperature in the converted output shows the benefit of the appreciable spectral separation between the quantum band and the noisy pump band.

4. DISCUSSION

The results demonstrate frequency tuning of true single photons emitted from a specific InAs QD. However, the underlying phase-matching condition can, in principle, be satisfied for any source emitting photons at any wavelength within the quantum band illustrated in Fig. 2(b). This has been verified experimentally through efficient frequency conversion of classical signals centered at 969 nm and 973 nm [22], 973.6 nm [31], and 982.1 nm [30], all using the same intermodal configuration as in this work. Efficient conversion across a range of input wavelengths is therefore readily achievable with this process. The primary challenge, as illustrated in Fig. 4(b), is not tuning the accepted input wavelength itself, but rather increasing the spectral separation between the input and output wavelengths within the quantum band. Overcoming this limitation is crucial, as it currently restricts the ability to bring spectrally distinct quantum emitters into resonance. As a result, the technique is confined mainly to devices with similar design parameters and consequently, similar emission wavelengths. Nevertheless, within these constraints, the method remains valuable for mitigating spectral distinguishability issues arising from inhomogeneous broadening among devices belonging to the same platform. While increased intra-band frequency detuning leads to a decrease in conversion efficiency, the efficiency is not similarly sensitive to the inter-band frequency separation. Consequently, we expect that conversion across 120 THz from the short-wavelength quantum band to the longer-wavelength telecom band can be performed with the same high peak effi-

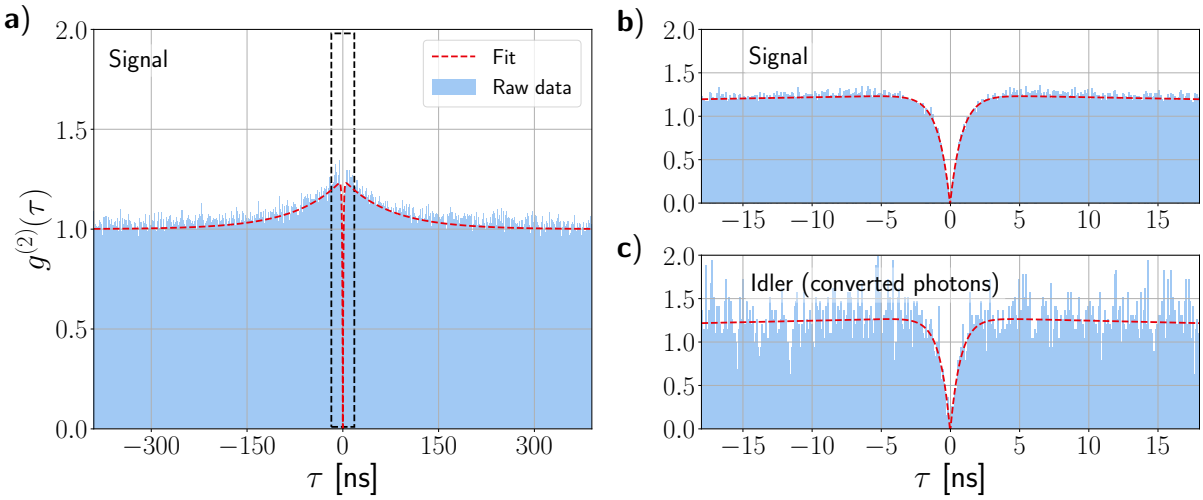

Fig. 5. Measurements of the second-order correlation function, $g^{(2)}(\tau)$. (a) Reference measurement of the quantum dot that was used as the signal. Bypassing the QFC setup, the recorded rate of single photons during the reference measurement was ~300 kcps. (b) Reference measurement zoomed in around zero coincidence time. The fit to Eq. (2) (red dashed lines) yields a low $g^{(2)}(0)$ of 0.010 ± 0.005 corresponding to a single-photon purity of 99%. (c) Same measurement for the idler (the converted photons), resulting in a $g^{(2)}(0)$ of $0.01^{+0.05}_{-0.01}$. Due to the losses incurred in the QFC setup (~9.5 dB), the recorded absolute rate of converted single photons for this measurement was ~1.5 kcps.

ciency (~85%) as exhibited in Fig. 4(b), if the frequencies of one of the pumps and the output single photon are interchanged. In this configuration, usually called distant Bragg scattering [23], the practical challenge becomes achieving sufficient isolation of the single photons from the noise in the spectral proximity of the pumps. This, again, motivates increasing the intra-band separation, because it then serves to separate the classical and quantum fields. Telecom-to-visible QFC via BS-FWM in such a configuration was recently demonstrated in a microresonator on a silicon nitride chip [21]. In the intermodal case outlined in this work, the span of intra-band detunings across which high-efficiency conversion can be achieved may be broadened by increasing the nonlinear interaction strength, for instance, by raising the available peak power beyond the 6.75 W per pump used here. This can either be done by an increase in the pump power, or by departing from the quasi-CW pumping scheme in favor of pulsed pumps with higher peak power. With increased pump power, the QFC process requires a shorter nonlinear interaction length. If the fiber is also shortened appropriately (to avoid back conversion), this in turn both expands the phase-matching bandwidth and reduces the impact of longitudinal non-uniformity. The latter is the effect suspected of limiting the span of intra-band detunings achieved in the present work, whereas the former is expected to become a limitation as even larger intra-band detunings are considered. Additionally, broadband pumps enable phase-matched interaction across a broader range of frequency components. For these reasons, pulsed pumps can better facilitate the conversion of photons with wider spectral linewidth as recently demonstrated in [27]. Employing pulsed pumps also offers the possibility to do spectro-temporal reshaping of the single-photon wavepackets. Indeed, suppose the classical pump pulse envelopes can be arbitrarily defined (such as with optical arbitrary waveform generation, OAWG [53]), in that case, it is possible to map any arbitrary input photon wavefunction to any arbitrary output photon wavefunction via BS-FWM [23]. In this fashion, the single photons may be temporally stretched, compressed, or entirely reshaped during the process. Note that this kind of spectral-temporal wavefunction reshaping (applicable both in the time and frequency domains) does not imply spectral filtering of the input photon and can theoretically be done while maintaining high photon conversion probability. The outlined intermodal BS-FWM platform is especially well-suited for this as it relies solely on pumps operating at telecom wavelengths, for which temporal pulse shaping is already a highly mature technology.

5. CONCLUSION

In this work, we have demonstrated quantum frequency conversion of single photons using a flexible intermodal BS-FWM platform. The process is driven by two pumps in the telecom band, with the nonlinear medium being a multimode step-index fiber. The conversion was demonstrated to be tunable over a 5 THz range, achieving a high peak conversion efficiency of 85% across approximately 1 THz. This conversion span is sufficient to reliably bridge the spectral variations caused by inhomogeneous broadening in quantum light sources. Due to the 120 THz spectral separation between the high-power pumps and the input/output single photons, no significant contribution to the photon statistics due to added noise photons was detected in the quantum band during the conversion process, despite room temperature conditions, as evidenced by the low output $g^{(2)}(0)$ value of $0.01^{+0.05}_{-0.01}$. This shows the advantage of the large spectral span enabled by the intermodal BS-FWM process. Achieving the same tunability bandwidth and efficiency as demonstrated here is highly challenging via optomechanical or electrooptic effects, and is entirely prohibited in non-cascaded TWM. Therefore, the process of BS-FWM is a prominent candidate for enabling the interfacing of multiple quantum light sources operating at distinct wavelengths. In particular, the intermodal variant of BS-FWM provides a cost-effective and easily implementable approach to unlocking phase matching within new spectral regions for quantum signals, and the results of our investigation into the intermodal platform thus pave the way for scalable quantum architecture relying on versatile and efficient QFC. Going forward, the regime of more broadband,

high-repetition-rate pulsed pumps, coupled with a pulsed QD excitation scheme, should be further investigated. In addition to enabling wave-function shaping experiments, this approach would allow optimizing the temporal overlap between single photons and pump pulses. As a result, the absolute rate of converted output photons might be increased sufficiently to allow for feasible two-photon interference measurements. Furthermore, with the implementation of a sufficiently powerful pump laser operating within the short-wavelength band, the intermodal platform could be extended to support frequency conversion of single photons from the short-wavelength quantum band to the telecom band.

Funding. Danmarks Frie Forskningsfond (1032-00460B); Innovationsfonden (Grand Solutions case no. 2079-00040B); Villum Fonden (Grant no. 42100, Grant no. VIL53033); European Research Council (ERC-StG "TuneTMD" Grant no. 101076437 and ERC-CoG "Unity" Grant no. 865230).

Disclosures. The authors declare no conflicts of interest.

Data availability. All data generated and/or analyzed during this study are available from the corresponding author on reasonable request.

Supplemental document. See Supplement 1 for supporting content.

REFERENCES

1. V. S. Shchesnovich, "Partial indistinguishability theory for multiphoton experiments in multiport devices," Phys. Rev. A **91**, 013844 (2015).
2. R. Raussendorf and H. J. Briegel, "A one-way quantum computer," Phys. Rev. Lett. **86**, 5188–5191 (2001).
3. D. Bouwmeester, J.-W. Pan, K. Mattle, *et al.*, "Experimental quantum teleportation," Nature **390**, 575–579 (1997).
4. I. A. Walmsley and J. Nunn, "Editorial: building quantum networks," Phys. Rev. Appl. **6**, 040001 (2016).
5. H.-K. Lo, M. Curty, and B. Qi, "Measurement-device-independent quantum key distribution," Phys. Rev. Lett. **108**, 130503 (2012).
6. J.-W. Pan, D. Bouwmeester, H. Weinfurter, *et al.*, "Experimental entanglement swapping: entangling photons that never interacted," Phys. Rev. Lett. **80**, 3891–3894 (1998).
7. D. Cogan, Z.-E. Su, O. Kenneth, *et al.*, "Deterministic generation of indistinguishable photons in a cluster state," Nat. Photon. **17**, 324–329 (2023).
8. R. Uppu, F. T. Pedersen, Y. Wang, *et al.*, "Scalable integrated single-photon source," arXiv (2020).
9. H. Wang, Y.-M. He, T.-H. Chung, *et al.*, "Towards optimal single-photon sources from polarized microcavities," Nat. Photon. **13**, 770–775 (2019).
10. L. Fan, C.-L. Zou, M. Poot, *et al.*, "Integrated optomechanical single-photon frequency shifter," Nat. Photon. **10**, 766–770 (2016).
11. L. J. Wright, M. Karpiński, C. Söller, *et al.*, "Spectral shearing of quantum light pulses by electro-optic phase modulation," Phys. Rev. Lett. **118**, 023601 (2017).
12. A. P. Vandevender and P. G. Kwiat, "High efficiency single photon detection via frequency up-conversion," J. Mod. Opt. **51**, 1433–1445 (2004).
13. B. Da Lio, C. Faurby, X. Zhou, *et al.*, "A pure and indistinguishable single-photon source at telecommunication wavelength," Adv. Quantum Technol. **5**, 2200006 (2022).
14. M. T. Rakher, L. Ma, O. Slattery, *et al.*, "Quantum transduction of telecommunications-band single photons from a quantum dot by frequency upconversion," Nat. Photon. **4**, 786–791 (2010).
15. S. Zaske, A. Lenhard, C. A. Keßler, *et al.*, "Visible-to-telecom quantum frequency conversion of light from a single quantum emitter," Phys. Rev. Lett. **109**, 147404 (2012).
16. X. You, M. Zheng, S. Chen, *et al.*, "Quantum interference with independent single-photon sources over 300 km fiber," Adv. Photon. **4**, 066003 (2022).
17. C. J. McKinstrie, J. D. Harvey, S. Radic, *et al.*, "Translation of quantum states by four-wave mixing in fibers," Opt. Express **13**, 9131–9142 (2005).
18. A. Singh, Q. Li, S. Liu, *et al.*, "Quantum frequency conversion of a quantum dot single-photon source on a nanophotonic chip," Optica **6**, 563–569 (2019).
19. Q. Li, M. Davanço, and K. Srinivasan, "Efficient and low-noise single-photon-level frequency conversion interfaces using silicon nanophotonics," Nat. Photon. **10**, 406–414 (2016).
20. C. Joshi, A. Farsi, S. Clemmen, *et al.*, "Frequency multiplexing for quasi-deterministic heralded single-photon sources," Nat. Commun. **9**, 847 (2018).
21. S. Raghunathan, R. Oliver, Y. Zhao, *et al.*, "Telecom-to-visible quantum frequency converter on a silicon nitride chip," Opt. Quantum **3**, 329–334 (2025).
22. T. Ulvenberg, D. Bolotov, L. S. Rishøj, *et al.*, "Broadband and tunable frequency conversion using intermodal Bragg scattering," in *Conference on Lasers and Electro-Optics (CLEO)*, Charlotte, North Carolina, 2024, p. SF2Q.3.
23. C. J. McKinstrie, L. Mejling, M. G. Raymer, *et al.*, "Quantum-state-preserving optical frequency conversion and pulse reshaping by four-wave mixing," Phys. Rev. A **85**, 053829 (2012).
24. L. R. Murphy, M. J. Olszewski, P. Androvitsaneas, *et al.*, "Tunable frequency conversion in doped photonic crystal fiber pumped near degeneracy," Optica **11**, 1490 (2024).
25. K. A. G. Bonsma-Fisher, P. J. Bustard, C. Parry, *et al.*, "Ultratunable quantum frequency conversion in photonic crystal fiber," Phys. Rev. Lett. **129**, 203603 (2022).
26. H. J. McGuinness, M. G. Raymer, C. J. McKinstrie, *et al.*, "Quantum frequency translation of single-photon states in a photonic crystal fiber," Phys. Rev. Lett. **105**, 093604 (2010).
27. R. Tannous, P. J. Bustard, D. England, *et al.*, "Efficient quantum frequency translation of broadband single photons by bragg-scattering four-wave mixing," Optica Quantum **3**, 168–174 (2025).
28. J. Demas, P. Steinvurzel, B. Tai, *et al.*, "Intermodal nonlinear mixing with Bessel beams in optical fiber," Optica **2**, 14–17 (2015).
29. H. Wang, M.-Y. Chen, Y.-F. Zhu, *et al.*, "Few-mode step-index optical fibers with ultra-low bending losses," J. Russian Laser Res. **34**, 298–302 (2013).
30. D. Bolotov, L. Grüner-Nielsen, K. Rottwitt, *et al.*, "Efficient all-fiber broadband frequency conversion via intermodal Bragg scattering," in *2023 IEEE Photonics Society Summer Topicals Meeting Series (SUM)* (2023), pp. 1–2.
31. D. Bolotov, T. Ulvenberg, K. Rottwitt, *et al.*, "Efficient frequency conversion via a wide-spanning intermodal four-wave mixing Bragg scattering process," Opt. Express **33**, 4595–4603 (2025).
32. M. Esmann, S. C. Wein, and C. Antón-Solanas, "Solid-state single-photon sources: recent advances for novel quantum materials," Adv. Funct. Mater. **34**, 2315936 (2024).
33. L. Mejling, C. J. McKinstrie, M. G. Raymer, *et al.*, "Quantum frequency translation by four-wave mixing in a fiber: low-conversion regime," Opt. Express **20**, 8367–8396 (2012).
34. L. Mejling, D. S. Cargill, C. J. McKinstrie, *et al.*, "Effects of nonlinear phase modulation on Bragg scattering in the low-conversion regime," Opt. Express **20**, 27454–27475 (2012).
35. M. L. H. Korsgaard, J. G. Koefoed, and K. Rottwitt, "Raman effects in quantum frequency conversion using Bragg scattering," Phys. Rev. A **110**, 033508 (2024).
36. M. A. Foster, A. C. Turner, R. Salem, *et al.*, "Broad-band continuous-wave parametric wavelength conversion in silicon nanowaveguides," Opt. Express **15**, 12949–12958 (2007).
37. P. Akrami, L. G. Nielsen, L. S. Rishøj, *et al.*, "Fabrication of heat-induced long-period gratings for mode conversion in few-mode fibers," Proc. SPIE **11713** (2021), 1171308.
38. T. A. Birks, I. Gris-Sánchez, S. Yerolatsitis, *et al.*, "The photonic lantern," Adv. Opt. Photon. **7**, 107–167 (2015).
39. R. Hvidberg, R. Malureanu, A. Arduin, *et al.*, "Excitation of LP0,m modes in large-core step-index fibers using binary phase plates," in *Conference on Lasers and Electro-Optics (CLEO)* (2024), p. JW2A.72.

40. J. Demas, L. Rishøj, and S. Ramachandran, "Free-space beam shaping for precise control and conversion of modes in optical fiber," Optics Express **23**, 28531–28545 (2015).
41. K. Jespersen, Z. Li, L. Grüner-Nielsen, *et al.*, "Measuring distributed mode scattering in long, few-moded fibers," in *Optical Fiber Communication Conference*, Los Angeles, CA, 2012, p. OTh3I.4.
42. P. Lodahl, S. Mahmoodian, and S. Stobbe, "Interfacing single photons and single quantum dots with photonic nanostructures," Rev. Mod. Phys. **87**, 347–400 (2015).
43. M. V. Rakhlin, K. G. Belyaev, G. V. Klimko, *et al.*, "InAs/AlGaAs quantum dots for single-photon emission in a red spectral range," Sci. Rep. **8**, 5299 (2018).
44. S. Lefrancois, A. S. Clark, and B. J. Eggleton, "Optimizing optical Bragg scattering for single-photon frequency conversion," Phys. Rev. A **91**, 013837 (2015).
45. T. Ulvenberg, J. G. Koefoed, and L. S Rishøjet, "Impact of core radius fluctuations on four-wave mixing efficiency in optical fiber," in *2024 Conference on Lasers and Electro-Optics Pacific Rim (CLEO-PR)* (2024), pp. 1–2.
46. S. Mumtaz, R.-J. Essiambre, and G. P. Agrawal, "Nonlinear propagation in multimode and multicore fibers: Generalization of the Manakov equations," J. Light. Technol. **31**, 398–406 (2013).
47. Y. Xiao, R.-J. Essiambre, M. Desgroseilliers, *et al.*, "Theory of intermodal four-wave mixing with random linear mode coupling in few-mode fibers," Optics Express **22**, 32039–32059 (2014).
48. M. Guasoni, F. Parmigiani, P. Horak, *et al.*, "Intermodal four-wave mixing and parametric amplification in kilometer-long multimode fibers," J. Light. Technol. **35**, 5296–5305 (2017).
49. A. S. Clark, S. Shahnia, M. J. Collins, *et al.*, "High-efficiency frequency conversion in the single-photon regime," Opt. Lett. **38**, 947–949 (2013).
50. R. H. Brown and R. Q. Twiss, "Correlation between photons in two coherent beams of light," Nature **177**, 27–29 (1956).
51. G. Kiršanskė, H. Thyrrestrup, R. Daveau, *et al.*, "Indistinguishable and efficient single photons from a quantum dot in a planar nanobeam waveguide," Phys. Rev. B **96**, 165306 (2017).
52. R. Brouri, A. Beveratos, J.-P. Poizat, *et al.*, "Photon antibunching in the fluorescence of individual color centers in diamond," Opt. Lett. **25**, 1294–1296 (2000).
53. S. T. Cundiff and A. M. Weiner, "Optical arbitrary waveform generation," Nat. Photon. **4**, 760–766 (2010).